Journal of Materials Science & Technology 157 (2023) 1–10

Contents lists available at ScienceDirect

Journal of Materials Science & Technology

journal homepage: www.elsevier.com/locate/jmst

Research Article

Hierarchical pomegranate-structure design enables stress management for volume release of Si anode

Fang Di[a], Zhenxing Wang[b,d], Chong Ge[a], Lixiang Li[a,c,*], Xin Geng[a,c], Chengguo Sun[a], Haiming Yang[a,c], Weimin Zhou[a,c], Dongying Ju[c], Baigang An[a,c,*], Feng Li[b,*]

[a] Key Laboratory of Energy Materials and Electrochemistry Liaoning Province, School of Chemical Engineering, University of Science and Technology Liaoning, Anshan 114051, China
[b] Institute of Metal Research, Chinese Academy of Sciences, Shenyang 110016, China
[c] Hainan Provincial Key Lab of Fine Chemistry, School of Chemical Engineering and Technology, Hainan University, Haikou 570228, China
[d] Jihua Laboratory, Guangdong Province, Foshan 528200, China

ARTICLE INFO

Article history:
Received 10 January 2023
Revised 20 February 2023
Accepted 22 February 2023
Available online 24 March 2023

Keywords:
Stress management
Silicon anode
Hierarchical structure
Covalent bonding
Volume release

ABSTRACT

Si is a promising anode material for lithium-ion batteries owing to its high theoretical capacity. However, large stress during (de)lithiation induces severe structural pulverization, electrical contact failure, and unstable solid-electrolyte interface, which hampers the practical application of Si anode. Herein, a Si-based anode with a hierarchical pomegranate-structure (HPS-Si) was designed to modulate the stress variation, and a sub-micronized Si-based sphere was assembled by the nano-sized Si nanospheres with sub-nanometer-sized multi-phase modification of the covalently linked SiO_{2-x}, SiC, and carbon. The sub-micronized HPS-Si stacked with Si nanospheres can avoid agglomerates during cycling due to the high surface energy of nanomaterials. Meanwhile, the reasonable pore structure from SiO_2 reduction owing to density difference is enough to accommodate the limited volume expansion. The Si spheres with a size of about 50 nm can prevent self-cracking. SiO_{2-x}, and SiC as flexible and rigid layers, have been synergistically used to reduce the surface stress of conductive carbon layers to avoid cracking. The covalent bonding immensely strengthens the link of the modification with Si nanospheres, thus resisting stress effects. Consequently, a full cell comprising an HPS-Si anode and a $LiCoO_2$ cathode achieved an energy density of 415 Wh kg^{-1} with a capacity retention ratio of 87.9% after 300 cycles based on the active materials. It is anticipated that the hierarchical pomegranate-structure design can provide inspiring insights for further studies of the practical application of silicon anode.

1. Introduction

With the rapid popularization of electric vehicles and the construction of large-scale energy storage systems, lithium-ion batteries (LIBs) with high energy and power density are highly expected [1–3]. Si has been regarded as one of the most promising candidates for the next generation of LIBs for its high theoretical capacity of 4200 mAh g^{-1}, the rational redox potential of 0.4 V vs. Li^+/Li, and natural abundance [4]. Nevertheless, the dramatic volume change accompanied by (de)lithiation of Si particles gives rise to a large stress, which leads to a series of mechanical failures: (i) Si particle cracks and pulverization; (ii) repeated formation of solid electrolyte interface (SEI) films; and (iii) loss of electrical contact with the current collector. All these issues cause fast capacity fading of the Si anode during repeated cycling. Until now, stress management strategies focused on size, surface modification, and buffer space construction, have been achieved by addressing the critical issues from significant anode volume expansion upon lithiation [5,6].

Although nanosized Si (~150 nm) can prevent self-cracking under large stress, mutual stress between Si particles can result in the delamination of electrode materials from the current collectors [7,8]. Meanwhile, large stress induces undesirable continuous SEI growth, which leads to the consumption of electrolytes, lengthening the Li-ion diffusion distances, and bringing about severe electrochemical performance degradation [9,10]. Considering that such mechanical failures largely originate from stress intensification during volume expansion, it is important to improve cycling stability through stress management. For example, as a mechanical confinement layer, SiO_2 has been used to prevent the change in the outer volume of the Si nanotubes because of its high mechanical

* Corresponding authors.
E-mail addresses: lxli2005@126.com (L. Li), bgan@ustl.edu.cn (B. An), fli@imr.ac.cn (F. Li).

https://doi.org/10.1016/j.jmst.2023.02.014
1005-0302/

strength [11]. Furthermore, SiC [12], TiO_2 [13], and TiO_{2-x} [14] with higher mechanical strength are also used as robust surface coatings to achieve Si stress dispersion during lithiation, while the SiC layer can prevent the carbon layer from catalyzing the chemical reaction between the Si and $LiPF_6$, causing the degeneration of Si anode [15]. It is well known that SiO_{2-x} can be used as the active component to store lithium ions [16]. Nevertheless, when the ratio of SiO_{2-x} is beyond 3 wt%, it leads to an increase in the irreversible capacity of the composites due to the reaction with lithium to form Li_xSiO_y [17]. However, as a modified layer, Li_xSiO_y with good flexible properties is beneficial to facilitate stress relaxation [18]. The modified layer is an effective strategy for stress management. Nevertheless, the interfacial interaction between the modified layers and Si is still an issue affecting the stability of Si-based anode [19]. When a weak interaction between the layers suffers the cycled volume change, the modified layers will inevitably lose the link with Si, which loses the protection of the layers for the anode [20]. Construction of the buffer space to accommodate the volume expansion of the Si anode is another essential strategy to relax the stress, such as hollow [21], hierarchical porous [22], and yolk-shell structures [23]. Such sufficient free volume takes advantage of stable SEI formation with reduced mechanical failure and stable electrochemical behavior in repeated cycling. Nevertheless, such strategy gives rise to large contacting resistance for the point contact between Si and conductive materials [24]. Also, the redundant space causes a low volumetric energy density of the battery [25].

In this study, a Si-based anode with hierarchical pomegranate-structure (HPS-Si) was designed to modulate the stress variation, a sub-micronized Si sphere was assembled by the nano-sized Si-based nanospheres with sub-nanometer-sized surface modification of the covalently linked SiO_{2-x}, SiC, and carbon. The sub-micronized HPS-Si stacked with Si nanospheres can avoid agglomerates during cycling because of its high surface energy of nanomaterials, and reasonable pore structure from SiO_2 reduction as a result of density difference enough to accommodate the limited volume expansion, which is confirmed by with the finite element model (FEM) and electrochemical analysis. The Si nanospheres with a size of about 50 nm can prevent from self-cracking. SiO_{2-x}, and SiC as flexible and rigid layers, have been used synergistically to reduce the surface stress of conductive carbon layers to avoid cracking. The covalent bonding showed its advantage in strengthening the link of the modified layers with Si particles to achieve the anode with good stability, which is attributed to the strong interface action that enhances the structural integrity and facilitates the reaction kinetics during the repeated cycles. The mechanical stress and strain in the multi-scale hierarchical structure can be easily relaxed without redundant space. Consequently, the HPS-Si owns high capacity and stability and exhibits excellent cycling stability as an anode of LIBs.

2. Experimental

2.1. Sample preparation

The synthesis of HPS-Si is schematically illustrated in Fig. 1. The SiO_2 spheres with a diameter of about 0.5 μm were synthesized via the modified Stober method with tetraethyl orthosil-

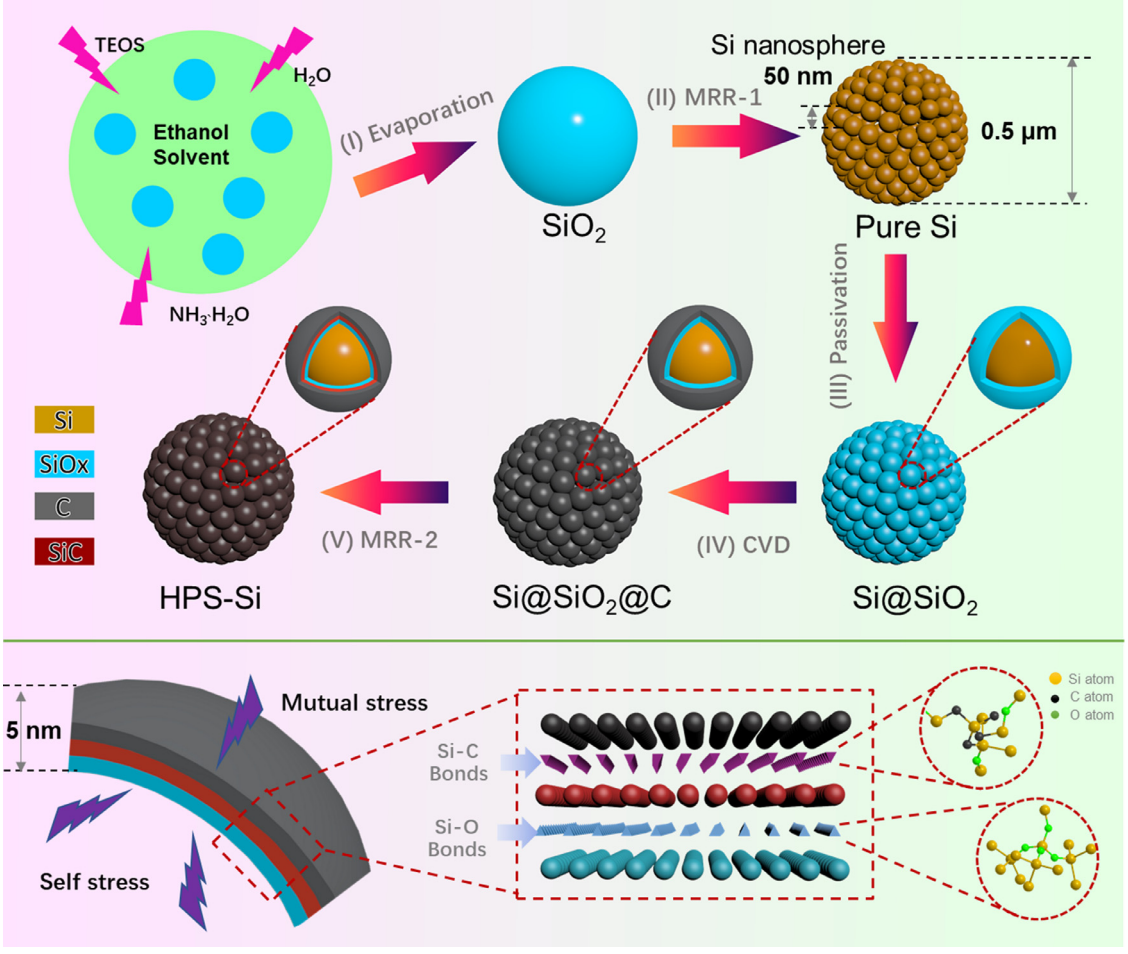

Fig. 1. Schematic diagram of the preparation process and hierarchical structure of the HPS-Si anode (TEOS: tetraethyl orthosilicate).

icate (TEOS) hydrolysis [26]. The first magnesiothermic reduction reaction (MRR-1) of SiO_2 spheres was used to prepare the Si pomegranate-like spheres (denoting as Pure Si) by the SiO_2 and Mg powders with a mass ratio of 5:4 in argon at 700 °C for 4 h, in which NaCl was added as a heat scavenger and template to avoid the formation of Mg_2SiO_4 and construct the unique pores [27]. To make the multi-phase modification around Si nanospheres, a series of processes of surface passivation, acetylene chemical vapor deposition (CVD), and MRR was carried out. Firstly, HPS-Si was passivated in air at 700 °C for 2 h in a tube furnace to produce a SiO_2 layer covering Si nanospheres (denoting as Si@SiO_2). Secondly, acetylene CVD technology was used to deposit the carbon layers on the surface of the Si@SiO_2, which produces the Si@SiO_2@C. The MRR was used again (MRR-2) to produce SiC and SiO_{2-x} layers by the Si@SiO_2@C and Mg powders with a mass ratio of 5:1. The MgO was removed by HCl solution (6.0 wt%). Finally, the sample was washed with deionized water, filtered, and dried in vacuum at 80 °C. The HPS-Si assembled by Si nanospheres with SiO_{2-x}, SiC, and carbon surface modification in turns.

2.2. Materials characterization

The composition and structure of Si-based materials were characterized by X-ray diffraction (XRD, Rigaku X'pret Powder, D/MAX-2500X, Cu K_α). The microstructure and morphology were observed by scanning electron microscope (SEM, FEI Apreo, operated at 5 kV) and transmission electron microscope (TEM, FEI Talos F200X, operated at 200 kV). The chemical states were analyzed by X-ray photoelectron spectroscopy (XPS, Axis Supra, Al K_α). The thermogravimetric analysis (TG, TA Instruments, TQ600) was performed in air atmosphere. Nitrogen physical adsorption isotherms were measured by a volumetric sorption analyzer (Micromeritics, ASAP2020). Pore size distribution (PSD) was analyzed according to the nonlocal density functional theory (NLDFT) method.

2.3. Electrochemical tests

The anodes were fabricated by casting a mixture of the active material of HPS-Si or Si@SiO_2@C, Super P, and carboxymethyl cellulose (CMC) with a weight ratio of 6:2:2 onto the copper foil. The foils loaded with the active materials were dried at 70 °C in vacuum oven overnight and punched to the disks with 12 mm in diameter. The mass loading of the active material for most electrodes was controlled to be about 0.50 mg cm^{-2}. Coin cells (2032 type) were assembled in an Ar-filled glovebox. The Pure Si, Si@SiO_2@C or HPS-Si electrode and a lithium metal disk were used as the working and the counter/reference electrode, and 1 M $LiPF_6$ dissolved in a mixture of ethylene carbonate (EC) and dimethyl carbonate (DMC) (1:1 in vol%) was used as the electrolyte. A potentiostat (Gamry3000) was used to test the cyclic voltammetry (CV) and electrochemical impedance spectroscopy (EIS). The cells were galvanostatically charged and discharged in the potential range of 0.01–1.5 V (vs. Li^+/Li) by an automatic battery testing system (LANHE CT3100). The galvanostatic intermittent titration technique (GITT) was used to measure the diffusion coefficient of lithium ions (D_{Li+}) of Si@SiO_2@C and HPS-Si samples at 0.1 A g^{-1} with a pulse time of 20 min and a relaxation time of 30 min. The calculation was done as below:

$$D_{Li+} = \frac{4L^2}{\pi\tau}\left(\frac{\triangle E_S}{\triangle E_\tau}\right)^2 \quad (1)$$

Based on Eq. (1), L represents the Li^+ diffusion length (equal to the electrode thickness, cm), τ stands for the relaxation time (s), ΔE_s represents the steady-state potential change via the cur-

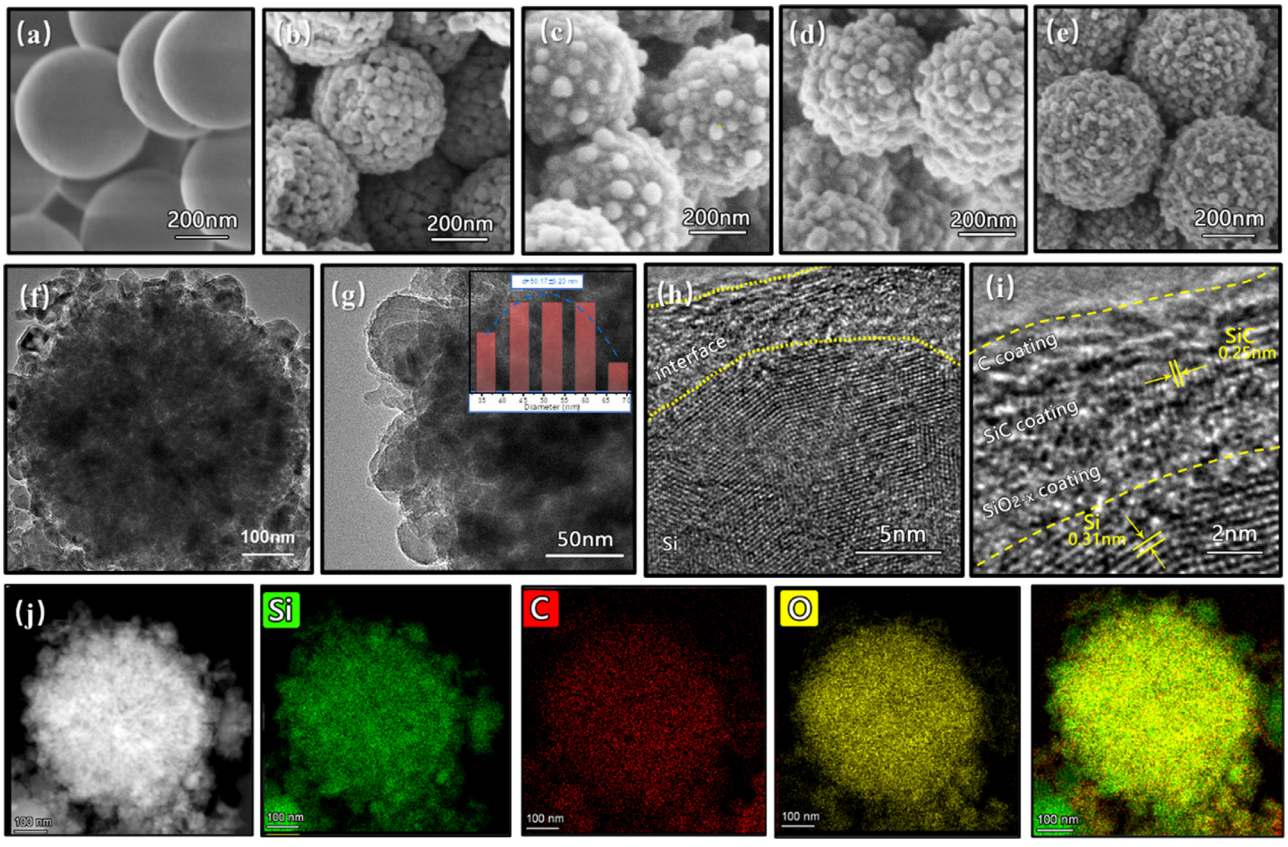

Fig. 2. SEM images of samples (a) SiO_2. (b) Pure Si. (c) Si@SiO_2. (d) Si@SiO_2@C. (e) HPS-Si. TEM images of (f, g) primary/secondary spherical structure, the inset is a size distribution plot of Si nanospheres. (h, i) Microstructure of nanoparticle inside HSP-Si. (j) Corresponding element mapping of Si, C, and O in HPS-Si.

rent pulse, and ΔE_τ is the potential change in current pulse after subtracting the iR drop. Full cells were assembled to further evaluate the performance of the HPS-Si electrode. The commercial $LiCoO_2$ served as the cathode, and the pre-lithiated HPS-Si electrode served as the anode. The pre-lithiation was enacted by discharging the above-mentioned half-cell at 0.1 A g^{-1} and the discharge cutoff potential to 0.01 V (vs. Li^+/Li). The fully discharged cell was disassembled in a glove box to investigate the pre-lithiated HPS-Si electrode. The capacity ratio of the negative/positive (N/P ratio) was 1.1:1, operating from 2.5 to 4.3 V.

2.4. Finite element model

Finite element simulations were conducted by a thermal-mechanical coupled model for stress distribution and the corresponding volumetric change evaluation of the experimental structure. The model was based on the results regarding TEM images with a 1/4 circular plane used to simulate the material expansion process and the axes of the circle are restricted to their radial displacements. In practice, the materials are tightly bonded to each other, and the bonding conditions are used in the finite elements with common nodal connections between multi-phase modifications of material. The analysis of volume suppression and stress management depends on the material properties of multi-phase modification, such as the modulus of Young and the ratio of Poisson.

3. Results and discussion

3.1. Morphology and microstructure

The morphology and structure of Si-based anodes were characterized by SEM to examine the evolution process. As shown in Figs. 2(a–e) and S1 in the Supporting Information, the SiO_2 prepared by the Stober method presents a spherical particle with a smooth surface and a diameter of about 0.5 μm. After the MRR-1 process, the smooth SiO_2 sphere is converted to the pomegranate-like sphere, which is composed of single Si nanospheres with a diameter of 50 nm (Fig. 2(a, b)). During the MRR-1 transformation process, a large space or void will be obtained as SiO_2 possesses a smaller volumetric mass compared to Si. Notably, the following annealing, including the acetylene CVD and MRR-2, will not damage the original structure of Si nanospheres (Fig. 2(c–e)) owing to its unique structure. In contrast, commercial-independent SiO_2 nanoparticles and Si nanoparticles undergo obvious agglomeration for their high surface energy during MRR and air passivation process (Fig. S2).

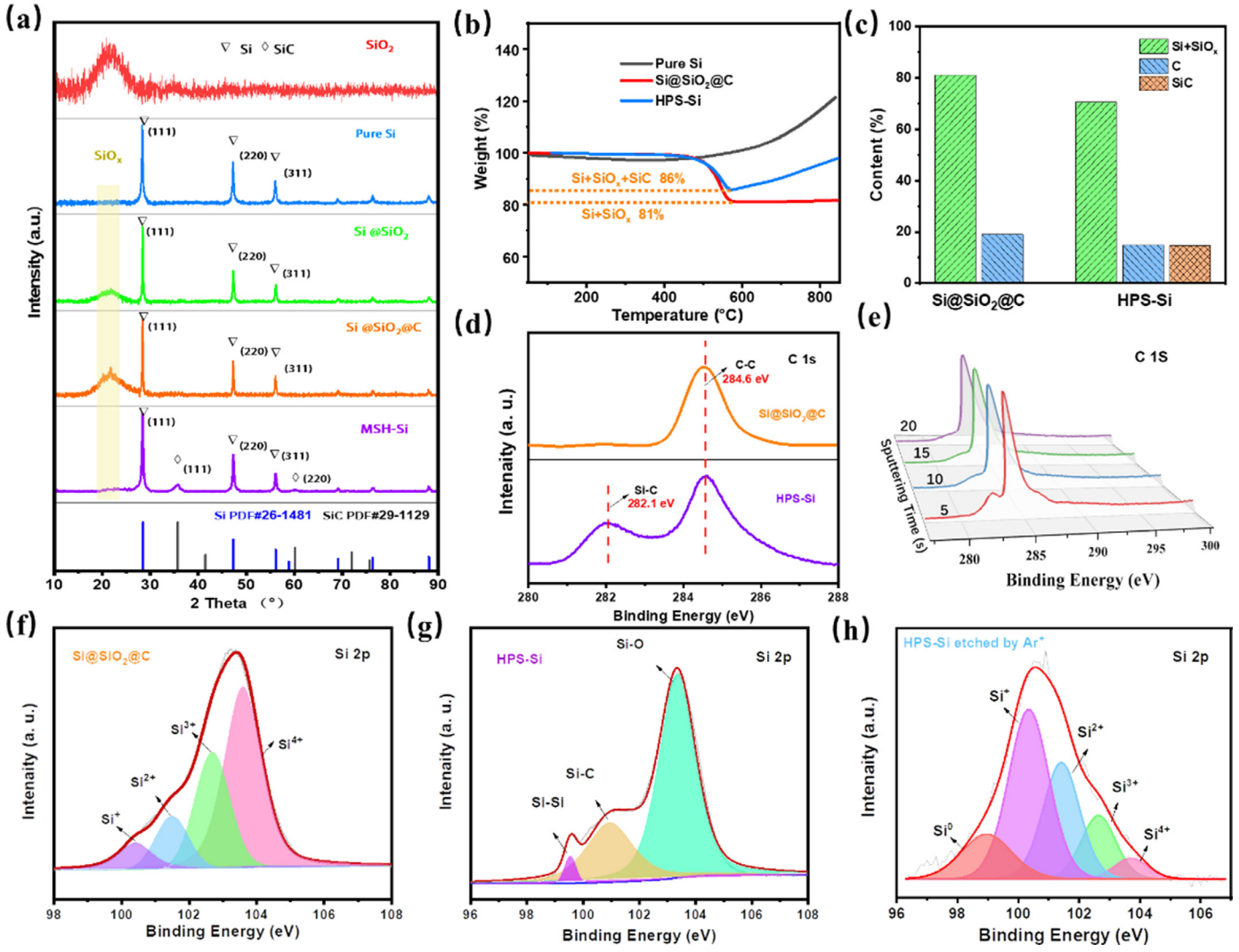

Fig. 3. (a) XRD patterns of samples. (b) TG curves of samples. (c) Phase ratio histogram of samples. (d) XPS survey spectra, C 1s of the Si@SiO_2@C and HPS-Si. (e) C 1s depth profiling XPS core spectra by Ar^+ sputtering of HPS-Si. (f, g) XPS survey spectra, Si 2p of the Si@SiO_2@C and HPS-Si. (h) XPS spectrum of the Si 2p of the HPS-Si sample etched 20 s by Ar^+.

As shown in Fig. 2(f, g), HPS-Si shows a sphere with a diameter of about 0.5 μm, containing many nanoparticles with large voids inside and the average size of Si nanospheres is around 50 nm, which provides enough space for relieving the volume expansion. The lattice fingerprint of the nanoparticle corresponds to the polycrystalline Si and surface modification (Fig. 2(h)). The Si is covered by the layers of SiO_{2-x}, SiC, and amorphous carbon in turns (Figs. 2(i) and S3). The elemental mapping of HPS-Si (Fig. 2(j)) shows that the Si element is intensively distributed in the nanospheres, accompanied by the oxygen and carbon that mainly derived from the outer layers of SiO_{2-x}, SiC, and amorphous carbon.

3.2. Composition and interface interaction

The phase composition of materials from SiO_2 to HPS-Si was examined by XRD (Fig. 3(a)). The amorphous SiO_2 by the modified Stober method is converted into polycrystalline Si after the MRR-1 process (Eq. (2)), which can be confirmed by the XRD characteristic peaks. Notably, the broad peak of amorphous SiO_2 disappears, indicating a transformation from SiO_2 to Si. The subsequent air passivation treatment on the Si results in the formation of the SiO_2 layer (Eq. (3)), which is indicated by the broad peak around 23° [28]. After the CVD on the passivated Si nanospheres, the broader peak around 23° resulted from overlapping peaks of the amorphous carbon layer and the SiO_2 layer can be discerned. To produce the SiC layer, MRR-2 on Si@SiO_2@C was used. The characteristic peaks around 35.9°, 60.2°, and 72.8° corresponding to the crystal faces of (111), (220), and (311) of β-SiC can be observed. The SiC is attributed to the interfacial reaction between the SiO_2 layer and the amorphous carbon layer (Eq. (4)) since it is thermodynamically favorable to form SiC rather than Si when the amorphous carbon exists [29,30]. Finally, XRD results further confirm that HPS-Si consists of Si, SiO_{2-x}, SiC, and carbon.

$$SiO_2 + Mg \rightarrow Si + MgO \quad (2)$$

$$Si + O_2 \rightarrow SiO_2 \quad (3)$$

$$SiO_2 + C + Mg \rightarrow SiO_{2-x} + SiC + MgO \quad (4)$$

The composition and carbon contents of samples were investigated by thermogravimetry (TG). As shown in Fig. 3(b), the Si sphere (black curve) shows a weight change at about 500 °C as the oxidation of Si into SiO_2. The Si@SiO_2@C (red curve) begins a

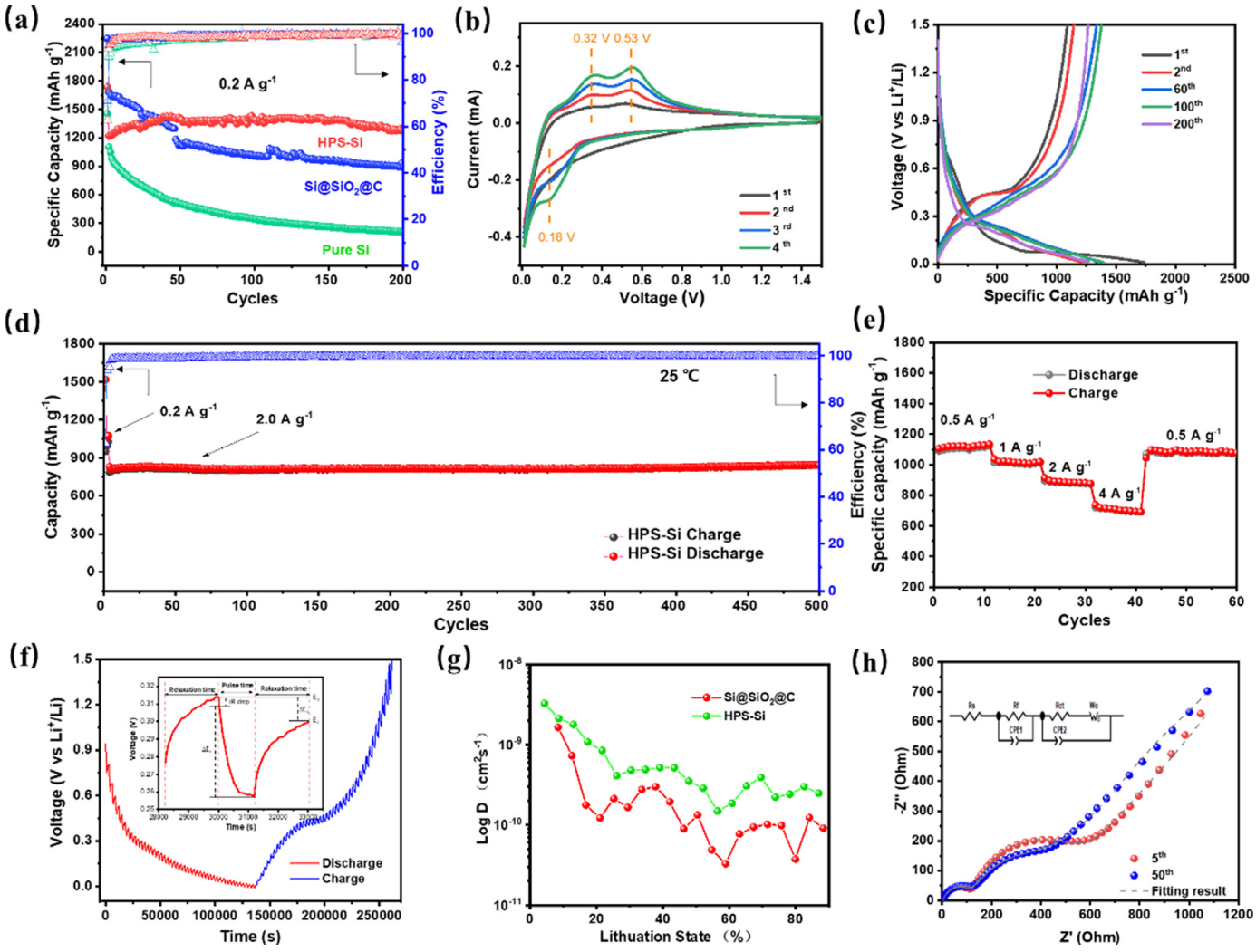

Fig. 4. (a) Cycling-induced variation of discharge capacity and CE for Pure Si, Si@SiO_2@C, and HPS-Si at 0.2 A g^{-1} for 200 cycles. (b) CV curves of HPS-Si at 0.2 mV s^{-1}. (c) Discharge-charge curves of HPS-Si at 0.2 A g^{-1}. (d) Cycling performance of HPS-Si at 2.0 A g^{-1} for 500 cycles in the 25 °C. (e) The rate capability of HPS-Si at current density from 0.5 to 4.0 A g^{-1}. (f) GITT curves of HPS-Si electrode (discharge-charge state), the inset is *E* vs *T* profile for one GITT test and (g) The diffusion coefficient of Li^+ during the discharge process for the Si@SiO_2@C and HPS-Si electrodes. (h) Nyquist plots of the HPS-Si electrode at the 5th and 50th cycles, the inset is an equivalent circuit for fitting impedance plot.

weight loss at about 460 °C as the reaction of the amorphous carbon, the carbon content is estimated to be about 19.0 wt%. There only is a small weight increase after 600 °C, indicating the dense SiO_2 layer preventing the inner Si from oxidation. HPS-Si (blue curve) also shows a 14.0 wt% weight loss at about 460 °C owing to the carbon oxidation. The decrease in carbon ratio in HPS-Si relative to Si@SiO_2@C is mainly attributed to the MRR between the amorphous carbon layer and the SiO_2 layer that consumes a part of carbon. The SiC can be estimated to be 14.6 wt% according to the amount of carbon. Meanwhile, the MRR is beneficial for the reduction of SiO_2 to SiO_{2-x}, accompanied by a higher carbon ratio. The Si content is estimated by the total content of Si and SiO_{2-x} in the sample, the results are shown in Fig. 3(c), it is about 80.0 and 72.5 wt% for Si@SiO_2@C and HPS-Si.

The porosity of samples is demonstrated in Fig. S4 and Table S1. All the samples exhibit typical type-IV isotherms (Fig. S4(a)), suggesting a mesoporous structure. The pore size distribution curves (Fig. S4(b)) confirm that the pore size ranges from 5 to 100 nm. Such large voids are principally produced during the conversion of SiO_2 to Si in virtue of the difference in the volumetric mass [31,32]. Moreover, HPS-Si has a significant formation of small mesopores with a size of 2–5 nm, which is attributed to the SiO_{2-x} and SiC formation between the layers of SiO_2 and carbon by MRR-2. These mesopores are helpful to alleviate volumetric expansion during the lithiation of Si and small mesopores can facilitate ion transport to improve the rate performance of the HPS-Si anode. Meanwhile, the hierarchical pomegranate-structure crosslinks the above carbon layers to construct a three-dimensional conductive network in order to guarantee the transfer of electrons between the surfaces and interfaces of the composite material (Fig. S5).

The cyclic stability of the Si anode can be improved by alleviating the volume expansion and enhancing the interaction be-

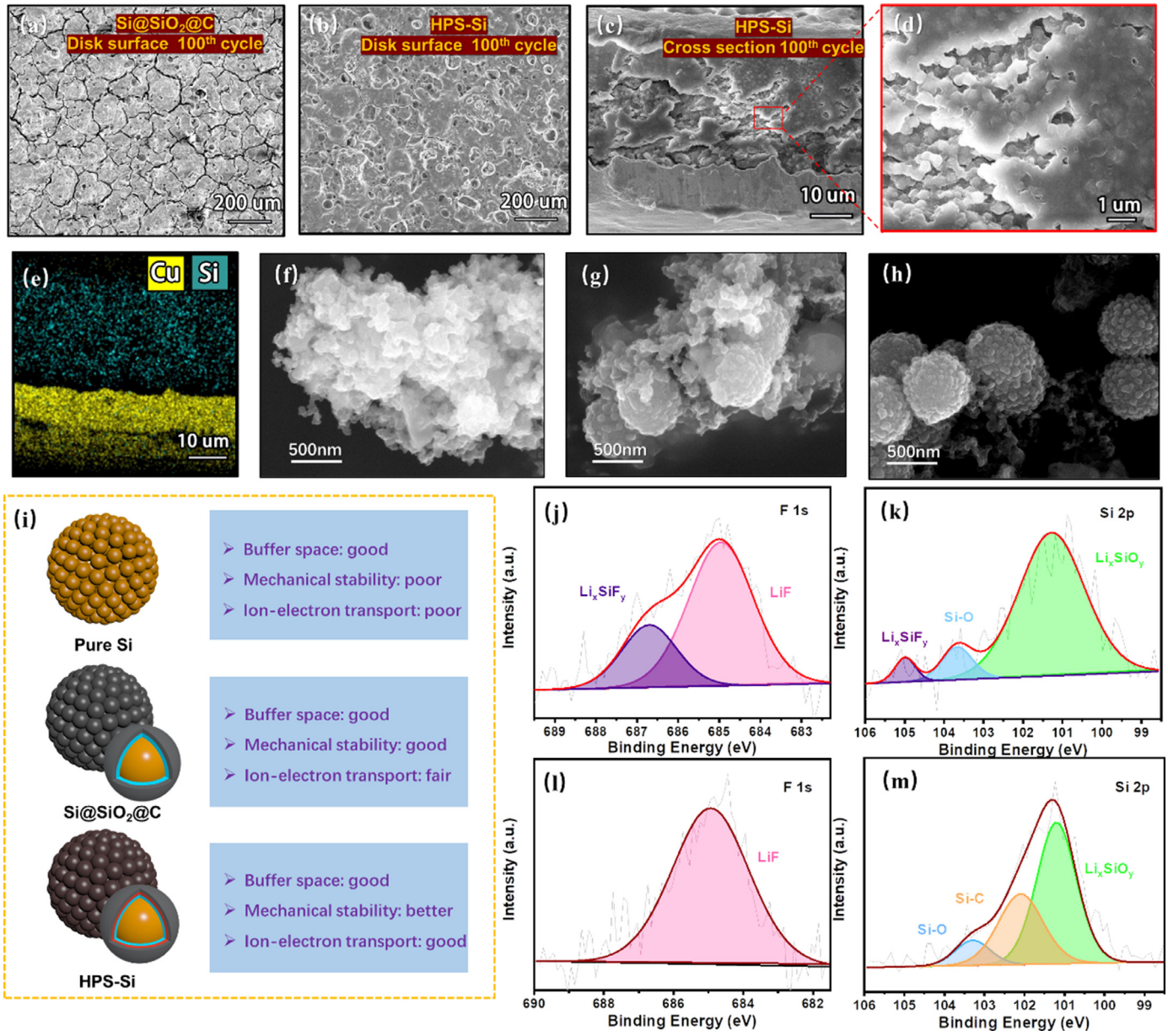

Fig. 5. (a, b) SEM images of the anode surface of Si@SiO_2@C and HPS-Si after 100 cycles. (c) SEM images of cross-sectional observation of HPS-Si electrode and (d) partial SEM image of Fig. 5(c). (e) Corresponding Cu and Si element mapping of Fig. 5(c). (f–h) SEM images of Pure Si, Si@SiO_2@C, and HPS-Si after 100 cycles. (i) Schematic diagram of the corresponding advantages and drawbacks of Pure Si, Si@SiO_2@C, and HPS-Si. (j, k) F 1s and Si 2p XPS spectra of Si@SiO_2@C anode after 100 cycles. (l, m) F 1s and Si 2p XPS spectra of HPS-Si anode after 100 cycles.

tween the modified layers. In fact, each modified layer around Si is produced through the mechanochemical process. The SiO_2 layer is formed by the oxidation of Si, and the SiC layer is produced through the MRR-2 between the interface of the SiO_2 and the carbon. Therefore, it can be deduced that each layer is chemically bonded through the interface. X-ray photoelectron spectroscopy (XPS) was further used to confirm the interface interaction between the modified layers. As shown in Fig. S6, the peaks at the binding energy of 101.5, 152.6, 284.6, and 531.6 eV are corresponding to Si 2p, Si 2s, C 1s, and O 1s, respectively. Notably, an additional peak at a binding energy of 100.9 eV in HPS-Si confirms the C-Si bond that derives from the SiC and the interaction between the SiC and the carbon (Fig. 3(d, e)) [33]. The XPS spectrum of the Si 2p region (Fig. 3(g)) proves the Si–Si, Si–C, and Si–O bands of HPS-Si around 99.0, 100.9, and 102.6 eV, respectively. Moreover, as shown in Fig. 3(f, h), HPS-Si containing Si element with a chemical value of Si^{4+} (103.6 eV), Si^{3+} (102.7 eV), Si^{2+} (101.7 eV), Si^{+} (100.6 eV), Si^{0} (99.4 eV) verify the transition from SiO_2 to SiO_{2-x} [34,35]. Such a transition from Si^{4+} to Si° further suggests the chemical bonding between the layers of Si, SiO_{2-x}, and SiC.

3.3. Electrochemical performance

As shown in Fig. 4(a), the cycle life curves of Pure Si, Si@SiO_2@C, and HPS-Si at 0.2 A g^{-1} for 200 cycles, the cell of HPS-Si keeps a stable capacity of 1272.8 mAh g^{-1} and more than 99% Coulombic efficiency (CE) even after 200 cycles, which is attributed to the good reversibility of (de)lithiation of HPS-Si anode. Fig. 4(b) shows the CV of the HPS-Si electrode, the cathodic peak around 0.18 V (vs. Li/Li^+) corresponds to the lithiation process of Si. During the charging process, two anodic peaks at about 0.32 and 0.53 V (vs. Li^+/Li) could be assigned to the delithiation processes of alloys that are the phase transition from $Li_{15}Si_4$ to amorphous Li_xSi and the subsequent transition from amorphous Li_xSi to Si [36]. Fig. 4(c) shows the potential profiles of the HPS-Si electrode at 0.2 A g^{-1} for the 1st, 2nd, 60th,100th, and 200th cycles. The initial discharge and charge capacities are 1737.8 and 1089.9 mAh g^{-1}. The first discharge exhibits a plateau below 0.10 V (vs. Li^+/Li) assigned to the lithiation process, which generally requires a large polarization in the first cycle [37], and the polarization decreases significantly as the cycling progresses. Rate and cycling stability were further ex-

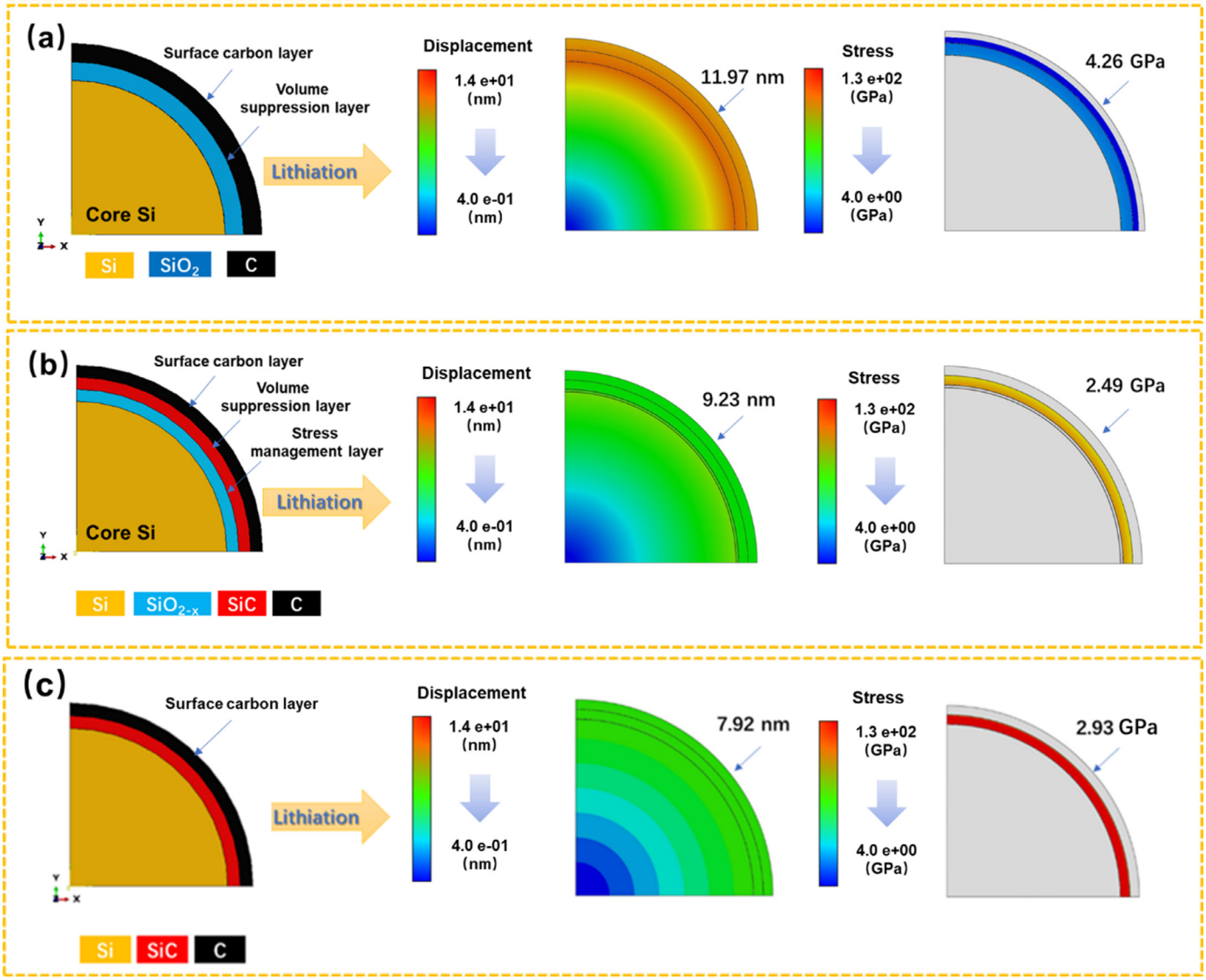

Fig. 6. Mechanical displacement and stress distribution during lithiation of (a) Si@SiO_2@C, (b) Si@SiO_{2-x}@SiC@C, (c) Si@SiC@C by FEM calculation (The value decreases from red to blue).

amined and the results are shown in Fig. 4(d). Even after 500 cycles, it maintains a capacity of 842.9 mAh g^{-1} with excellent capacity retention. In addition to a high capacity and an excellent cycling ability, HPS-Si also exhibits a good rate capability as shown by Fig. 4(e). The average reversible capacity of HPS-Si delivers 1100, 900, 800, 650, and 1100 mAh g^{-1} at 0.5, 1.0, 2.0, 4.0, and 0.5 A g^{-1}. The excellent cycling stability and rate performance of HPS-Si are attributed to the porosity and complete carbon layer promoting electrochemical kinetics, the HPS-Si relaxing the stress from volume release.

To acquire the kinetic behavior of the Si@SiO_2@C and HPS-Si, GITT measurements were carried out to get $D_{Li}{}^+$. As shown in Fig. 4(f, g), the diffusion coefficient of the HPS-Si electrode is significantly higher than Si@SiO_2@C at 0.1 A g^{-1}. As HPS-Si with more mesopores from the transition of SiO_2 to SiO_{2-x} compared to Si@SiO_2@C, it can make the unobstructed Li^+ transport. As an anode material of LIBs, HPS-Si is also beneficial to get a stable SEI film for the mechanical integrity of the overall structure. As the EIS shown in Fig. 4(h), the diameters of two semicircles of EIS represent the interfacial impedance of the SEI film (R_{SEI}) and the charge transfer impedance (R_{CT}), respectively [38]. The slope of the straight line in the low frequency represents the diffusion impedance of Li^+ in the electrode. R_{SEI} in the high-frequency range keeps stable from the 5th to 50th cycles, indicating stable SEI film formed onto HPS-Si. The significant decrease of R_{CT} in the middle-frequency range, suggests that the electric conductivity and charge transfer kinetics of the cycled electrode can be effectively improved by forming a hierarchical pomegranate-structure (Fig. S7).

3.4. Structure and interface integrity after cycles

To prove the stability of HPS-Si, the cycled cell was disassembled to observe the electrode morphology of Si@SiO_2@C and HPS-Si. As shown in Fig. 5(a, b), the Si@SiO_2@C electrode has visible cracks, which can block the particle contact and accelerate the separation from the current collector. The cross-sectional SEM images of the HPS-Si electrode demonstrate the good interface contact between the active material and the current collector, confirming that the volumetric stress can be alleviated by the mechanically stable multi-scale hierarchical structure (Fig. 5(c–e)). Furthermore, the structure of HPS-Si after 10, 50, and 100 cycles is well kept as shown in Fig. 5(h) and S8. In contrast, the Pure Si by direct MRR-1 of SiO_2 has completely lost the spherical structure (Fig. 5(f)). However, the situation is improved after the passivation and acetylene CVD on the Pure Si (Fig. 5(g)), the Si@SiO_2@C still presents a sphere consisting of nanoparticles despite a little structural damage. HPS-Si has significantly superior performance compared to Pure Si and Si@SiO_2@C (Fig. 5(i)). XPS (Fig. 5(j–m)) was further used to examine the composition of SEI of Si@SiO_2@C and HPS-Si after 100 cycles. According to Si 2p spectra, the formation of Li_xSiO_y by the reaction of SiO_{2-x} with electrolyte is beneficial for the stabilization of SEI film. Li_xSiF_y is only present in the Si@SiO_2@C sample based on F 1s and Si 2p spectra, confirming the SiC layer can inhibit the penetration of F^- to react with Si and SiO_{2-x} [14]. Since the production of Li_xSiF_y not only consumes electrolytes but also degrades the reversible capacity of the Si anode, the inhibition of the SiC layer on the penetration of F^- can help the HPS-Si anode to get better cycling stability.

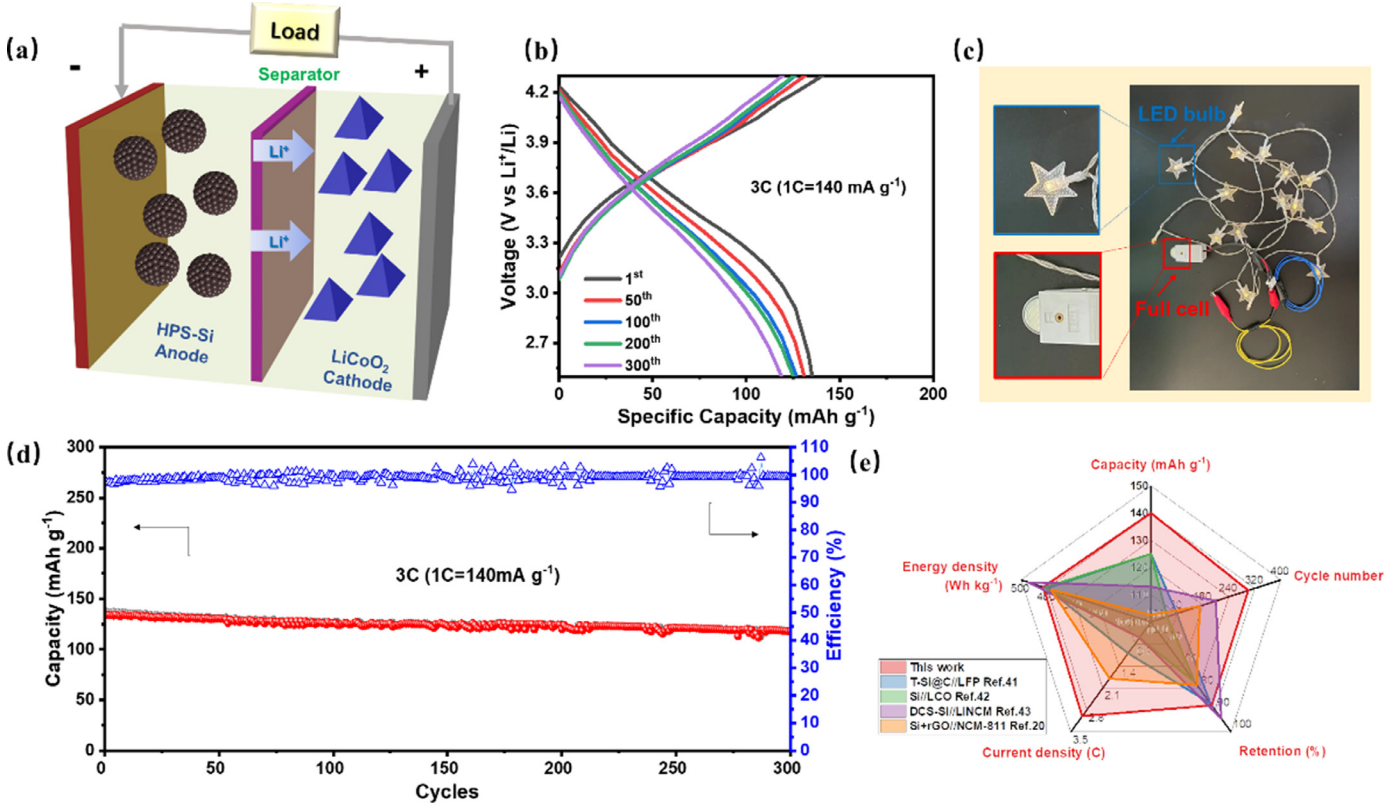

Fig. 7. (a) Schematic illustration of Li-ion cell assembled by HPS-Si anode and $LiCoO_2$ cathode. (b) Voltage profiles of the full cell at the 1st, 50th, 100th, 200th, and 300th cycles. (c) The digital photo of the light strip lit by the full cell. (d) Cycling performance of the full cell at 3C for 300 cycles. (e) Comparison of electrochemical performance of Si-based full cell with previous reports.

3.5. Hoop stress distribution by FEM calculation during lithiation

To explore the stress management of surface modification, the FEM based on TEM images ($r = 25$ nm) was performed to calculate mechanical displacement and stress distribution during lithiation (Fig. 6). The material properties such as modulus of Young and ratio of Poisson refer to the previous reports (Table S2) [39,40]. Fig. S9 shows the hoop surface displacements of the Si model after full lithiation (V_{LixSi}: $V_{Si} = 3.8$). For the Si@C model (Fig. S10), drastic volume expansion (374%) caused by lithiation leads to the experience of compressive stress by volume expansion of Si inside the particle while simultaneously generating tensile stress (5.56 GPa) at the carbon surface layer, and large mechanical stress can crack the carbon surface layer. For Si@SiO_2@C and Si@SiO_{2-x}@SiC@C models (Fig. 6(a, b)), the surface displacement is significantly reduced by 14% and 33%, respectively, which is attributed to the suppression of volume expansion by SiO_2 and SiC, while simultaneously generating tensile stress at the carbon surface layer is 4.26 and 2.49 GPa, respectively. Compared to the Si@SiC@C model, the Si@SiO_{2-x}@SiC@C has relatively low compressive stress due to the contribution of SiO_{2-x} to the stress relaxation (Fig. 6(c)). The carbon layer is below the acceptable stress limits, which is in full accord with the SEM images of cycled HPS-Si in Fig. S8. As a result, it is believed that the HPS-Si with lower surface displacement and compressive stress during lithiation has the advantage of preserving the morphological integrity, which leads to a stable mechanical structure during cycling. The advantages of multi-phase modification in the interface stability and the inhibition of volume expansion were well verified. In addition, the hierarchical pomegranate-structure can effectively adjust the volume expansion and has a more suitable buffer space. Therefore, HPS-Si owns a stronger ability to maintain interfacial stability and high volumetric energy density, as shown in Fig. S11.

3.6. Full cell performance

The HPS-Si||$LiCoO_2$ cell assembled according to the model shown in Fig. 7(a). Fig. 7(b) displays representative the discharge-charge curves of the full cell in the 1st, 50th, 100th, 200th, and 300th cycles at 3 C (1 C = 140 mA g^{-1}) in the voltage window of 2.5 to 4.3 V, which shows an average discharge plateau around 3.7 V and an initially reversible capacity of 133.4 mAh g^{-1}. Even after 300 cycles, the full cell exhibits excellent stability with a capacity retention of 87.9% (Fig. 7(d)). As shown in Fig. 7(c), the strip of lights was lighted by an HPS-Si||$LiCoO_2$ button cell. The HPS-Si||$LiCoO_2$ cell exhibits a high specific energy density of about 415 Wh kg^{-1} based on the weight of cathode and anode materials. The full cell assembled by HPS-Si anode and $LiCoO_2$ cathode shows superior or comparable performance compared with the Si-based full cells previously reported (Fig. 7(e)), illuminating the potential application of HPS-Si material for LIBs [20,41–43].

4. Conclusions

In summary, a hierarchical pomegranate structure with stress management mechanisms, comprising a sub-micronized Si-based sphere assembled by the nano-sized Si nanospheres with covalently linked sub-nanometer-sized surface modification was proposed. To improve the mechanical stability and ion-electron transport, an effective strategy by integrating free space, particle size, multi-phase modification, and interfacial force of the composite was designed. In this configuration, the unique porous structure and nano-sized particles can avoid self-cracking during (de)lithiation. The covalently linked multi-phase modification effectively strengthens stress relaxation and interfacial interaction, which is confirmed by FEM simulation and various analytical tools. SiO_{2-x} plays a critical role in mitigating stress intensification, SiC with rigid feature functions the modulation of volume changes during lithiation, and the complete external carbon layer ensures the electric conductivity of the electrode. Consequently, a full cell comprising an HPS-Si anode and a $LiCoO_2$ cathode successfully confirmed the commercial feasibility. The energy density of 415 Wh kg^{-1} with a capacity retention ratio of 87.9 % after 300 cycles was achieved. The promising application of HPS-Si in lithium-ion batteries is further demonstrated by assembling the full cell that exhibits comparable or superior performance compared with the typical Si-based full cells.

Declaration of Competing Interest

The authors report no declarations of interest.

Acknowledgments

Financial support by the NSFC Nos. 51972156, 51872131, 51672117, 51672118, 22209055, CPSF No. 2022M721330, and Distinguished Professor of Liaoning Province (2017) are acknowledged.

Supplementary materials

Supplementary material associated with this article can be found, in the online version, at doi:10.1016/j.jmst.2023.02.014.

References

[1] F.X. Wu, J. Maier, Y. Yu, Chem. Soc. Rev. 49 (2020) 1569–1614.
[2] Y.L. An, Y. Tian, H. Wei, B.J. Xi, S.L. Xiong, J.K. Feng, Y.T. Qian, Adv. Funct. Mater. 30 (2019) 1908721–1908734.
[3] C.G. Sun, Z.X. Wang, L.C. Yin, S.J. Xu, Z.A. Ghazi, Y. Shi, B.G. An, Z. Sun, H.-M. Cheng, F. Li, Nano Energy 75 (2020) 104976–104985.
[4] C.Z. Zhang, F. Wang, J. Han, S. Bai, J. Tan, J.S. Liu, F. Li, Small Struct. 2 (2021) 2100009–21000027.
[5] X.S. Shen, Z.Y. Tiana, R.J. Fan, L. Shao, D.P. Zhang, G.L. Cao, L. Kou, Y.Z. Bai, J. Energy Chem. 27 (2018) 1067–1090.
[6] S. Park, J. Sung, S. Chae, J. Hong, T. Lee, Y. Lee, H. Cha, S.Y. Kim, J.J. Cho, ACS Nano 14 (2020) 11548–11557.
[7] X.H. Liu, J.Y. Huang, Energy Environ. Sci. 4 (2011) 3844–3860.
[8] X.-L. Wu, Y.-G. Guo, L.-J. Wan, Chem.-Asian J. 8 (2013) 1948–1958.
[9] J.Y. Ma, J. Sung, Y. Lee, Y. Son, S. Chae, N. Kim, S.H. Choi, J. Cho, Adv. Energy Mater. 10 (2020) 1903400.
[10] K.W. Schroder, A.G. Dylla, S.J. Harris, L.J. Webb, K.J. Stevenson, ACS Appl. Mater. Interfaces 6 (2014) 21510–21524.
[11] H. Wu, G. Chan, J.W. Choi, I. Ryu, Y. Yao, M.T. McDowell, S.W. Lee, A. Jackson, Y. Yang, L.B. Hu, Nat. Nanotechnol. 7 (2012) 310–315.
[12] D.T. Ngo, H.T.T. Le, X.M. Pham, C.N. Park, C.J. Park, ACS Appl. Mater. Interfaces 9 (2017) 32790–32800.
[13] S. Fang, L.F. Shen, G.Y. Xu, P. Nie, J. Wang, H. Dou, X.G. Zhang, ACS Appl. Mater. Interfaces 6 (2014) 6497–6503.
[14] Y.L. Yu, G. Li, X. Chen, W.G. Lin, J.F. Rong, W.S. Yang, RSC Adv. 8 (2018) 15094–15101.
[15] C.H. Yu, X. Chen, Z.X. Xiao, C. Lei, C.X. Zhang, X.Q. Lin, B.Y. Shen, R.F. Zhang, F. Wei, Nano Lett. 19 (2019) 5124–5132.
[16] Y.M. Ju, J.A. Tang, K. Zhu, Y. Meng, C.Z. Wang, G. Chen, Y.J. Wei, Y. Gao, Electrochim. Acta 191 (2016) 411–416.
[17] H. Uono, B.C. Kim, T. Fuse, M. Ue, J. Yamaki, J. Electrochem. Soc. 153 (2006) A1708–A1713.
[18] J. Sung, J. Ma, S.H. Choi, J. Hong, N. Kim, S. Chae, Y. Son, S.Y. Kim, J. Cho, Adv. Mater. 31 (2019) 1900970–1900979.
[19] S.J. Fan, H. Wang, J.F. Qian, Y.L. Cao, H.X. Yang, X.P. Ai, F.P. Zhong, ACS Appl. Mater. Interfaces 12 (2020) 16411–16416.
[20] Q.S. Wang, T. Meng, Y.H. Li, J.D. Yang, B.B. Huang, S.Q. Ou, C.G. Meng, S.Q. Zhang, Y.X. Tong, Energy Storage Mater. 39 (2021) 354–364.
[21] T. Yoon, T. Bok, C. Kim, Y. Na, S. Park, K.S. Kim, ACS Nano 11 (2017) 4808–4815.
[22] M. Cui, L. Wang, X.W. Guo, E.R. Wang, Y.B. Yang, T.H. Wu, D. He, S.Q. Liu, H.J. Yu, J. Mater. Chem. A 7 (2019) 3874–3881.
[23] Y.J. Liu, Z.X. Tai, T.F. Zhou, V. Sencadas, J. Zhang, L. Zhang, K. Konstantinov, Z.P. Guo, H. Liu, Adv. Mater. 29 (2017) 1900970–1900979.
[24] X.H. Zhang, D.H. Wang, X.Y. Qiu, Y.J. Ma, D.B. Kong, K. Mullen, X.L. Li, L.J. Zhi, Nat. Commun. 11 (2020) 3826–3834.
[25] L. Zhang, C.R. Wang, Y.H. Dou, N.Y. Cheng, D.D. Cui, Y. Du, P.R. Liu, M. Al-Mamun, S.Q. Zhang, H.J. Zhao, Angew. Chem.-Int. Edit. 58 (2019) 8824–8828.
[26] W. Stober, A. Fink, E. Bohn, Science 26 (1968) 62–69.
[27] F. Di, N. Wang, L.X. Li, X. Geng, H.M. Yang, W.M. Zhou, C.G. Sun, B.G. An, J. Alloy. Compd. 854 (2021) 8–15.

[28] G.W. Hu, R.H. Yu, Z.H. Liu, Q. Yu, Y.Y. Zhang, Q. Chen, J.S. Wu, L. Zhou, L.Q. Mai, ACS Appl. Mater. Interfaces 13 (2021) 3991–3998.
[29] X.Y. Liu, H.W. Zhao, S. Jiang, S. Wu, T. Zhao, L.X. Li, X. Geng, H.M. Yang, W.M. Zhou, C.G. Sun, Y.Q. Chen, B.G. An, J. Alloy. Compd. 881 (2021) 160442–160450.
[30] J.M. Zhang, J.J. Tang, X.Y. Zhou, M. Jia, Y.P. Ren, M. Jiang, T.J. Hu, J. Yang, Chem-electrochem 6 (2019) 450–455.
[31] Y.G. Zhang, N. Du, Y.F. Chen, Y.F. Lin, J.W. Jiang, Y.H. He, Y. Lei, D.R. Yang, Nanoscale 10 (2018) 5626–5633.
[32] D.T. Ngo, H.T.T. Le, X.M. Pham, J.W. Jung, N.H. Vu, J.G. Fisher, W.B. Im, I.D. Kim, C.J. Park, J. Mater. Chem. A 6 (2018) 2834–2846.
[33] M. Dasog, L.F. Smith, T.K. Purkait, J.G.C. Veinot, Chem. Commun. 49 (2013) 7004–7006.
[34] M. Dasog, C. Rachinsky, J.G.C. Veinot, J. Mater. Chem. 21 (2011) 12422–12427.
[35] Y.R. Ren, M.Q. Li, J. Power Sources 306 (2016) 459–466.
[36] J. Han, X.N. Tang, S.F. Ge, Y. Shi, C.Z. Zhang, F. Li, S. Bai, J. Mater. Sci. Technol. 80 (2021) 259–265.
[37] J. Liu, P. Kopold, P.A. van Aken, J. Maier, Y. Yu, Angew. Chem.-Int. Edit. 54 (2015) 9632–9636.
[38] B. Philippe, R. Dedryvere, J. Allouche, F. Lindgren, M. Gorgoi, H. Rensmo, D. Gonbeau, K. Edstrom, Chem. Mater. 24 (2012) 1107–1115.
[39] Y.F. Zhang, Y.J. Li, Z.Y. Wang, K.J. Zhao, Nano Lett. 14 (2014) 7161–7170.
[40] Y.S. Choi, M. Pharr, K.H. Oh, J.J. Vlassak, J. Power Sources 294 (2015) 159–166.
[41] T.S. Mu, S.F. Lou, N.G. Holmes, C.H. Wang, M.X. He, B.C. Shen, X.T. Lin, P.J. Zuo, Y.L. Ma, R.Y. Li, C.Y. Du, J.J. Wang, G.P. Yin, X.L. Sun, ACS Appl. Mater. Interfaces 13 (2021) 4093–4101.
[42] Z. Yi, N. Lin, Y.Y. Zhao, W.W. Wang, Y. Qian, Y.C. Zhu, Y.T. Qian, Energy Storage Mater. 17 (2019) 93–100.
[43] S.Q. Chen, L.F. Shen, P.A. van Aken, J. Maier, Y. Yu, Adv. Mater. 29 (2017) 1605650–1605657.